Research Article

Nano Research
2023, 16(2): 2428–2435

ISSN 1998-0124 CN 11-5974/O4
https://doi.org/10.1007/s12274-022-4980-4

Porous needle-like Fe-Ni-P doped with Ru as efficient electrocatalyst for hydrogen generation powered by sustainable energies

Yue Wang[1,§], Zhi Chen[1,§], Qichang Li[1], Xinping Wang[1], Weiping Xiao[2], Yunlei Fu[3], Guangrui Xu[4], Bin Li[4], Zhenjiang Li[4], Zexing Wu[1] (✉), and Lei Wang[1,3] (✉)

[1] *Key Laboratory of Eco-chemical Engineering, International Science and Technology Cooperation Base of Eco-chemical Engineering and Green Manufacturing, College of Chemistry and Molecular Engineering, Qingdao University of Science and Technology, Qingdao 266042, China*
[2] *College of Science, Nanjing Forestry University, Nanjing 210037, China*
[3] *Shandong Engineering Research Center for Marine Environment Corrosion and Safety Protection, College of Environment and Safety Engineering, Qingdao University of Science and Technology, Qingdao 266042, China*
[4] *College of Materials Science and Engineering, Qingdao University of Science and Technology, Qingdao 266061, China*
[§] *Yue Wang and Zhi Chen contributed equally to this work.*

Received: 15 June 2022 / **Revised:** 30 July 2022 / **Accepted:** 28 August 2022

ABSTRACT

Electrocatalytic water electrolysis, involving hydrogen evolution reaction (HER) and oxygen evolution reaction (OER), two half-reactions, is an eco-friendly approach toward hydrogen production. In this work, needle-like Ru-Fe-Ni-P on NiFe foam is prepared through corrosive engineering and following a low-temperature phosphorization procedure for overall water-splitting. The as-designed Ru-Fe-Ni-P exhibits a porous needle-like structure, surface, and binder-free merits, and then can expose rich active sites, favor the transportation of mass/electron, and accelerate the reaction kinetics during catalytic process. Then, the synthesized Ru-Fe-Ni-P owns remarkable catalytic performance for HER, with 18 and 67 mV to reach 10 mA·cm^{-2} in alkaline and neutral media. Moreover, a low cell voltage of 1.51 V is required to produce a current of 10 mA·cm^{-2} in a two electrode electrolyzer with excellent stability. Interestingly, sustainable energies can power the electrolyzer effectively with abundant hydrogen generation.

KEYWORDS

metal phosphide, needle-like morphology, hydrogen generation, overall water splitting

1 Introduction

Increasing global environmental and energy problems have prompted intensive research on clean, sustainable alternative energy sources with natural abundant and environmental friendly merits [1–7]. Hydrogen (H_2) is considered as promising energy to substitute the carbon-intensive fuels and alleviate energy-crisis owing to the weight–energy density, renewable nature, and eco-friendly [8–12]. Electrochemical water splitting, powered by sustainable energies (wind, solar, and thermal sources), is commonly regarded as a cost–effective and clean way for producing huge quantities of hydrogen [13–18]. Nevertheless, the slow kinetics of electrode reactions for water-splitting, including cathodic hydrogen evolution reaction (HER) and anodic oxygen evolution reaction (OER), increased the costs of hydrogen [19, 20]. Until now, noble metals (Pt and IrO_2) are the sate-of-the-art electrocatalysts toward water-splitting. However, the scarcity limited their practical utilizations [21]. Thus, tremendous attentions have paid to designing electrocatalysts, including vacancy engineering [22], strain engineering [23], and nanostructure regulating [24], have been exploited to obtain electrocatalysts with trace loading of noble metals and non-precious metals electrocatalysts [25].

At present, non-precious metal-based catalysts are attracted extensive attentions, such as transition metal (TM) [26] TM oxides (TMO) [27–29], TM nitrides (TMN) [30, 31], TM phosphides (TMP) [32–34], TM carbides (TMC) [35, 36], and TM sulfides (TMS) [37, 38]. Among them, TMP-based electrocatalysts exhibit high electrical conductivity, quick charge transfer, and favorable reaction kinetics, and then attract particular attentions for electrochemical water splitting [39]. Various approaches have emerged to further improve the catalytic activity, such as morphological modulation [40, 41], elemental doping [42], and interfacial engineering [43]. In general, morphology engineering is an efficient approach to optimizing the catalytic performance of the as-synthesized samples by providing more active sites and accelerating the mass transport. Therefore, various morphologies, including nanosphere [44], nanorod [45], and nanosheet [46], are developed in energy-related fields. However, surfactant and complicated procedures are generally required to obtain the designed nanostructure. Apart from nanostructure modulation, elemental doping can create new active sites, decrease the electrical resistance and regulate the electronic structure. For instance, phosphorus doping into the base surface of tungsten

Address correspondence to Zexing Wu, splswzx@qust.edu.cn; Lei Wang, inorchemwl@126.com

disulfide can effectively improve the hydrogen evolution [47]. It is reported that the incorporation of trace amounts of Ru into TMS can improve the catalytic performance of catalysts [48]. Experimental and theoretical calculations also have shown that Ru exhibits significant adsorption of hydrogen and oxygen containing intermediates [49]. Therefore, developing facile approach to constructing electrocatalyst with specific morphology and elemental doping would be a pressing task.

In this work, a simple and practical avenue is developed to synthesize needles like Ru-Fe-Ni-P and Fe-Ni-P, and study the electrochemical properties for HER and OER, respectively. The obtained vertical nanoarrays facilitated the exposure of the active sites and transportation of electron and electrolyte during electrocatalytic process. Moreover, the Fe-Ni phosphides species *in-situ* produced onto the porous NiFe foam also act as important role on boosting the catalytic HER/OER activities due to the excellent intrinsic activity and synergistic effect. Thus, the prepared Ru-Fe-Ni-P and Fe-Ni-P all show excellent catalytic activities with 18 and 188 mV toward 10 mA·cm^{-2} for HER and OER, respectively. Remarkably, a small voltage of 1.51 V is required to reach 10 mA·cm^{-2} with remarkable stability for overall water splitting.

2 Materials and methods

2.1 Synthesis of Ru-Fe-Ni

NiFe layered double hydroxide (LDH) was synthesized by a corrosion approach in the presence of chloride ion. Firstly, NiFe foam (1 × 1.5) cm^2 was cleaned by deionized water and then immersed into a solution containing 0.0879 g NaCl aqueous solution and stirred for 12 h. Following, the NiFe was washed several times by water and dried at 60 °C in a vacuum drying tank for 3 h to obtain NiFe LDH. The Ru-Fe-Ni was prepared by introducing 5 mg $RuCl_3{\cdot}xH_2O$.

2.2 Synthesis of Ru-Fe-Ni-P

The Ru-Fe-Ni and $NaH_2PO_2{\cdot}2H_2O$ were in the tube furnace, and then the tube furnace was heated to 350 °C and kept in Ar atmosphere for 2 h. After natural cooling, a precious metal-doped porous nickel-iron phosphide (Ru-Fe-Ni-P) was obtained.

3 Results and discussion

3.1 Materials characterizations

Figure 1(a) illustrates the synthetic process of Ru-Fe-Ni-P with a facile two-step approach, including ambient corrosive engineering and low-temperature phosphorization. The X-ray diffraction (XRD) patterns (Fig. S1 in the Electronic Supplementary Material (ESM)) demonstrates the synthesized catalysts are mainly composed by FeP_4 (PDF#79-0486), NiP (PDF#74-1382), and Ni_2P (PDF#03-0953). Relative to NiFe foam (Fig. S2 in the ESM), dense nanomaterials are homogeneously generated on NiFe foam with abundant voids after corrosive engineering and phosphorization treatment (Fig. 1(b)). The high-resolution scanning electron microscopy (SEM) images in Figs. 1(c) and 1(d) verify the needle-like morphology of the as-synthesized Ru-Fe-Ni-P with rich interconnected channels. The transmission electron microscopy (TEM) images (Figs. 1(e) and 1(f)) further reveal the needle-like morphology of Ru-Fe-Ni-P with numerous pores (yellow dotted circles). The formed pores facilitate the contact with electrolytes,

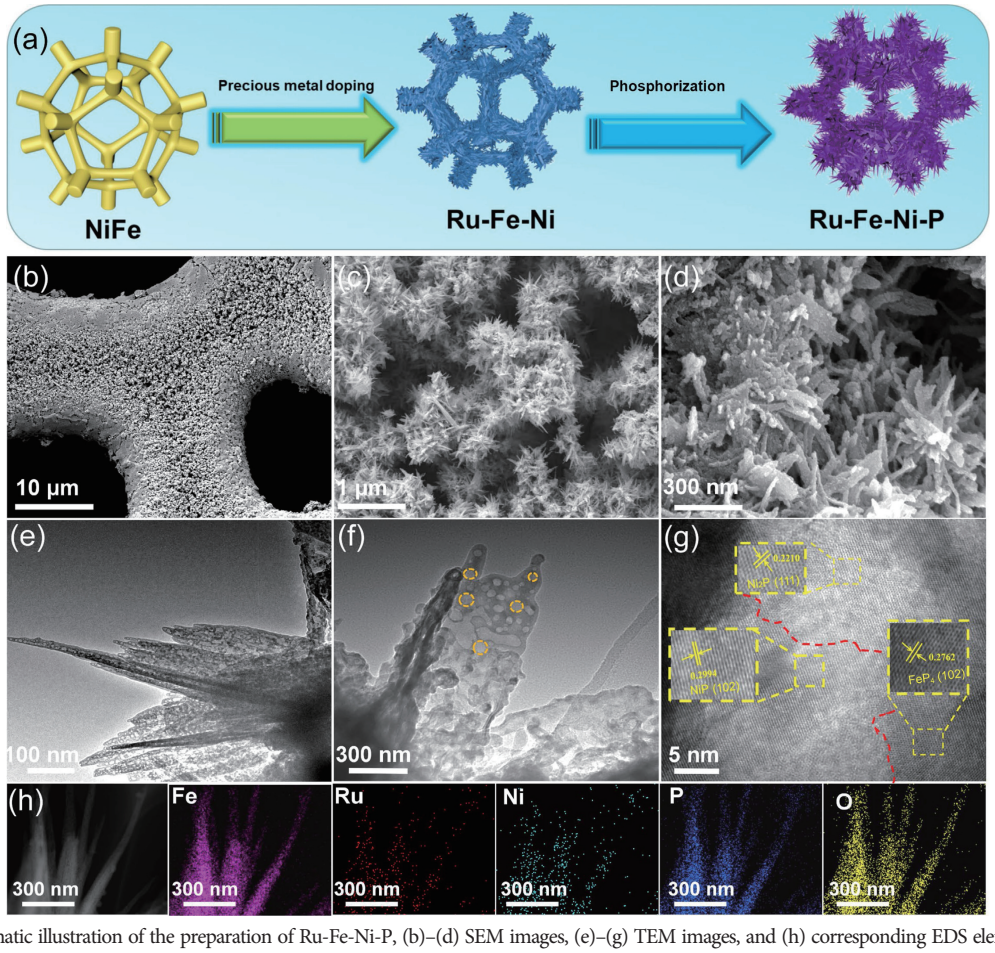

Figure 1 (a) Schematic illustration of the preparation of Ru-Fe-Ni-P, (b)–(d) SEM images, (e)–(g) TEM images, and (h) corresponding EDS elemental mappings of Fe, Ru, Ni, O, P in Ru-Fe-Ni-P.

favor the mass transfer, and accelerate produced bubbles release [50]. In addition, the formation of heterojunctions is confirmed by high-resolution TEM images, and the distinguished interface between NiP, Ni_2P, and FeP_4 is marked by a red dotted line. The heterostructure can expose more active sites, thus improving the catalytic performance [51]. The *d*-spacing of 0.2994, 0.2210, and 0.2762 nm are contributed to the (102), (111), and (131) facets of NiP, Ni_2P, and FeP_4 (Fig. 1(g)). Moreover, Ni, P, Fe, and Ru are uniformly distributed over the prepared electrocatalyst via the corresponding energy dispersive spectroscopy (EDS) elemental mappings (Fig. 1(h)).

As illustrated in Fig. 2(a), the X-ray photoelectron spectroscopy (XPS) survey spectrum verifies Ru, Ni, Fe, O, and P elements in the Ru-Fe-Ni-P. Similarly, the Fe-Ni-P is composed by Ni, Fe, O, and P elements, without doping of Ru in Fig. S3(a) in the ESM. In Ni 2p (Fig. 2(b)), the XPS peak of 856.6 eV represents the Ni $2p_{3/2}$ feature of Ni^{2+}, indicating the oxidation of the Ni_2P surface, thus forming phosphates; and the two situated at 853.5 and 861.9 eV are ascribed to Ni $2p_{3/2}$ [52–54], the two peaks in the region corresponding to the binding energy of $Ni^{\sigma+}$ in Ni_2P and satellite peaks, respectively. And the three peaks at 870.8, 873.9, and 879.2 eV are contributed to Ni $2p_{1/2}$ [55–57], corresponding to the binding energy of Ni–P, indicating the high oxidation state of Ni^{2+} overwhelmingly dominated in NiO–NiP and satellite peaks, respectively. For Fe 2p (Fig. 2(c)), peaks at 707.2 and 720.4 eV are ascribed to Fe $2p_{3/2}$ and Fe $2p_{1/2}$ [58, 59], and two peaks at 711.1 and 724.3 eV are contributed to Fe $2p_{3/2}$ and Fe $2p_{1/2}$ [60], corresponding to the binding energy of Fe–P and Fe^{3+}, respectively. And with satellite peaks at 728.5 and 715.3 eV [61, 62]. As illustrated in Fig. 2(d), the peaks of Ru 3p can be detected in the as-designed Ru-Fe-Ni-P. Two prominent peaks located at 483.9 and 461.5 eV are affiliated to Ru $3p_{1/2}$ and Ru $3p_{3/2}$ of Ru^0 [63, 64]. As for the P 2p, the binding energies at 129.7 eV correspond to the P $2p_{3/2}$ of P 2p (Fig. 2(e)) and the binding energies at 130.6 eV are ascribed to P $2p_{1/2}$ species, further demonstrating the formation of metal phosphides. Moreover, the binding energies at 134.1 and 131.9 eV for two peaks are due to exposure to air caused by surface oxidation and oxidation of P species [65]. The XPS analysis diagram, the proportion of these three components can be roughly calculated based on the information of elements and the proportion of them. The percent of every species, such as FeP_4, NiP, and Ni_2P, accounts for 7.96%, 0.43%, and 0.33%. We also insighted the XPS spectra of Fe–Ni–P without Ru incorporated (Fig. S3 in the ESM). In addition, the measurement of contact angles in Fig. 2(f) and Movie ESM1 are applied to estimate the hydrophilic of Ru-Fe-Ni-P and compared with NiFe and Ru-Fe-Ni (Fig. S4 in the ESM). The result confirms that Ru-Fe-Ni-P electrode exhibits superhydrophilic surface, guaranteeing the intimate contact with the electrolyte during the electrocatalytic reaction process.

3.2 Measurement of HER

The electrocatalytic performances were measured in 1 M KOH first. As displayed in Figs. 3(a) and 3(b) Ru–Fe–Ni–P heterostructure exhibits outstanding HER activity with low overpotentials of merely 18 and 75 mV to reach 10 and 50 $mA{\cdot}cm^{-2}$, respectively, which demonstrates the prominent catalytic activity of Ru-Fe-Ni-P toward HER (Fig. S5 in the ESM). The results show that the corrosion process and the coexistence of Ru and P elements play key role on improving the catalytic performance. Besides, Ru-Fe-Ni-P shows a small Tafel slope of 53 $mV{\cdot}dec^{-1}$, lower than NiFe (245 $mV{\cdot}dec^{-1}$), NiFe LDH (204 $mV{\cdot}dec^{-1}$), Fe-Ni-P (121 $mV{\cdot}dec^{-1}$), and Pt/C (75 $mV{\cdot}dec^{-1}$) (Fig. 3(c)), demonstrating its favorable reaction kinetics. The catalytic activity of as-prepared Ru-Fe-Ni-P is comparable to or surpasses most reported catalysts (Fig. 3(d) and Table S1 in the ESM). As shown in Figs. 3(e) and 3(f), the multiple-step chronopotentiometry and chronopotentiometry measurement exhibit negligible decay, verifying its excellent durability for HER.

Motivated by the excellent HER electrocatalytic activity in basic electrolyte, the HER electrocatalytic performance of Ru-Fe-Ni-P is studied in 1 M phosphate buffered saline (PBS). As illustrated in Figs. 4(a) and 4(b), Ru-Fe-Ni-P also displays a remarkable activity with 67 mV at 10 $mA{\cdot}cm^{-2}$, lower than NiFe (418 mV), NiFe LDH (351 mV), Fe-Ni-P (117 mV), and Pt/C (115 mV), It also presents a high mass activity. In Fig. 4(c), the Ru-Fe-Ni-P owns a Tafel slope of 79 $mV{\cdot}dec^{-1}$, smaller than NiFe (235 $mV{\cdot}dec^{-1}$), NiFe LDH (210 $mV{\cdot}dec^{-1}$), Fe-Ni-P (82 $mV{\cdot}dec^{-1}$), and Pt/C (92 $mV{\cdot}dec^{-1}$). In addition to the catalytic performance, the Ru-Fe-Ni-P presents long-term stability in neutral medium (Fig. 4(d)). The enhanced catalytic activity of Ru-Fe-Ni-P is comparable with

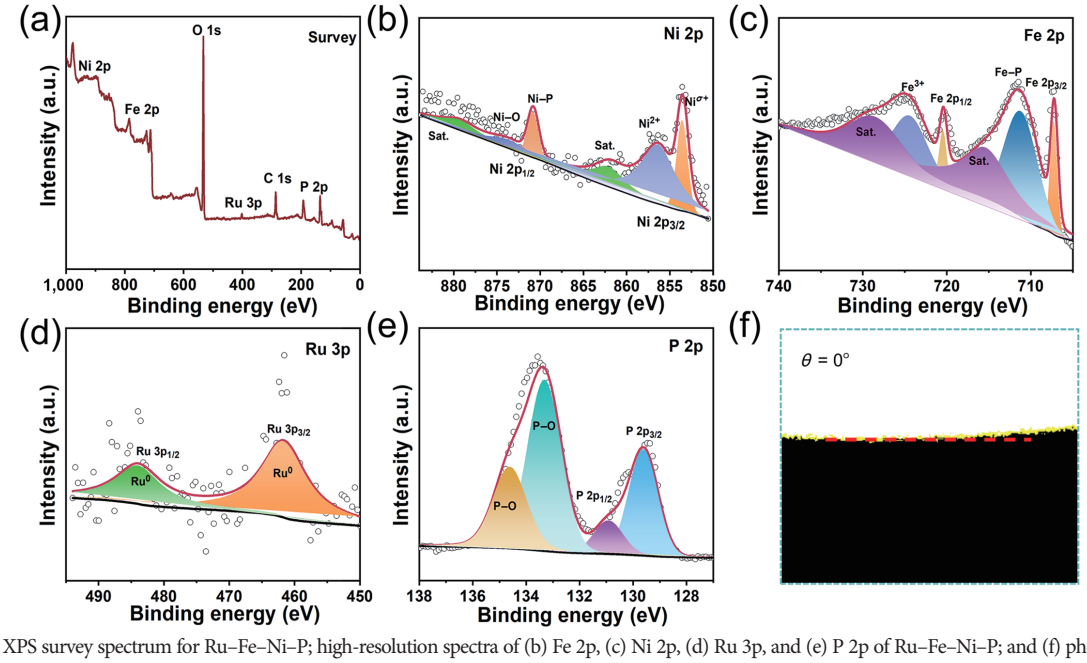

Figure 2 (a) XPS survey spectrum for Ru–Fe–Ni–P; high-resolution spectra of (b) Fe 2p, (c) Ni 2p, (d) Ru 3p, and (e) P 2p of Ru–Fe–Ni–P; and (f) photos of contact angles of Ru-Fe-Ni-P.

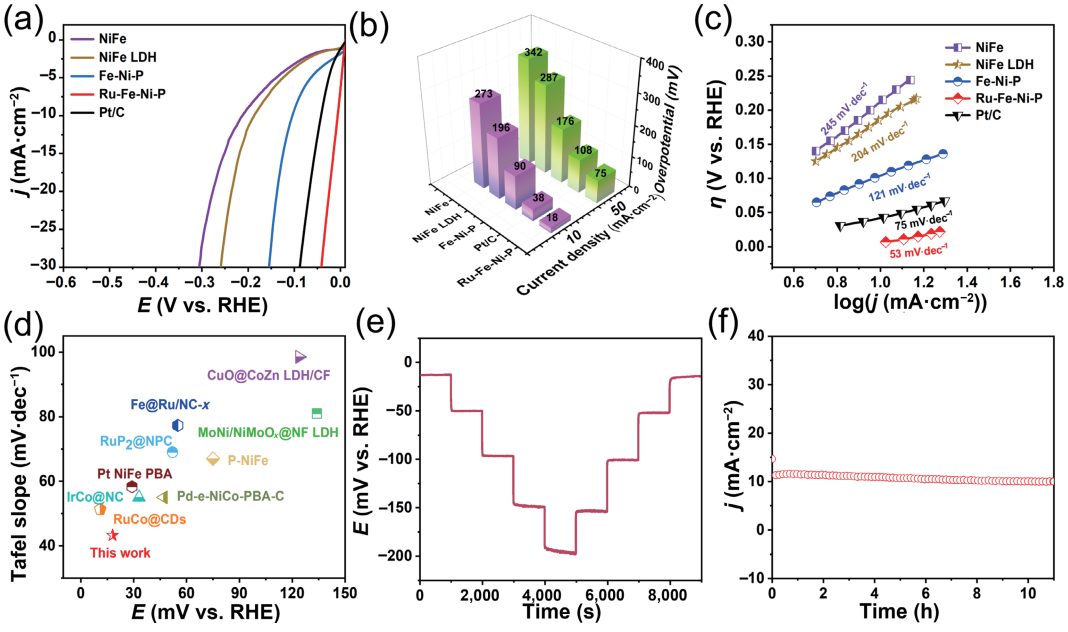

Figure 3 Electrochemical activities toward HER in alkaline electrolyte of 1 M KOH. (a) LSV curves of NiFe, NiFe LDH, Fe-Ni-P, Ru-Fe-Ni-P, and Pt/C. (b) Comparison of corresponding overpotentials at 10 and 50 mA·cm^{-2} of obtained catalysts. (c) Tafel plots of NiFe, NiFe LDH, Fe-Ni-P, Ru-Fe-Ni-P and Pt/C for HER. (d) Overpotentials at 10 mA·cm^{-2}. (e) The durability test of the Ru-Fe-Ni-P under different current densities. (f) Long-term stability test of Ru-Fe-Ni-P for HER.

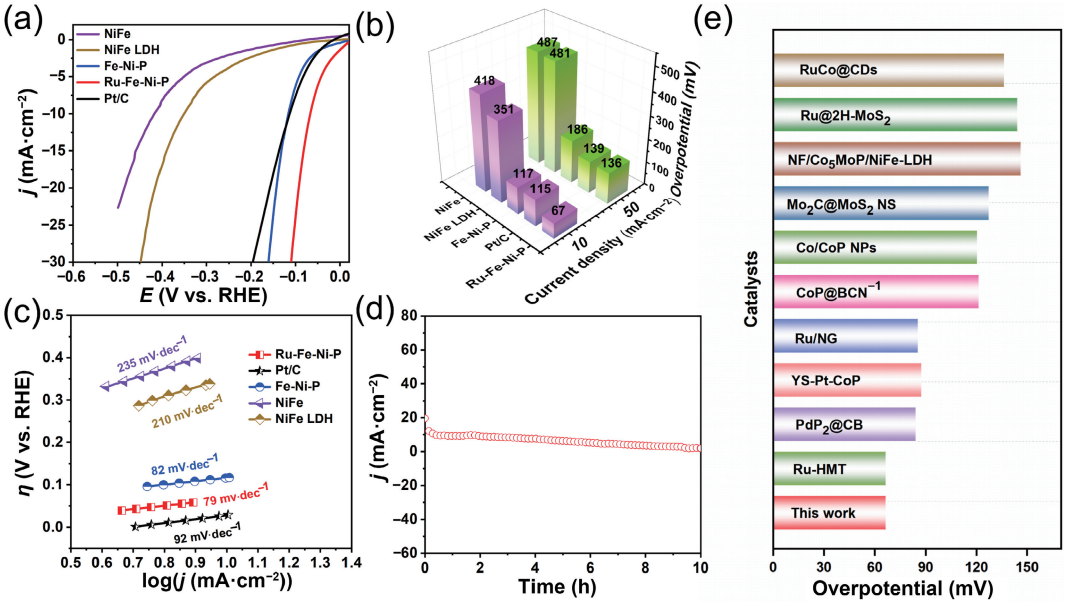

Figure 4 Electrochemical activities toward HER in 1 M PBS. (a) LSV curves of NiFe, NiFe LDH, Fe-Ni-P, Ru-Fe-Ni-P, and Pt/C for HER. (b) Comparison of corresponding overpotentials at 10 and 50 mA·cm^{-2} of obtained catalysts. (c) Tafel plots of NiFe, NiFe LDH, Fe-Ni-P, and Ru-Fe-Ni-P. (d) Long-term stability test of Ru-Fe-Ni-P at the current density of 10 mA·cm^{-2}. (e) Comparison of overpotentials at 10 mA·cm^{-2} with reported catalysts.

the reported catalysts (Fig. 4(e)). In addition, the synthetic conditions are optimized to regulate the catalytic performance (Fig. S6 in the ESM).

3.3 Measurement of OER

Figure 5(a) shows linear sweep voltammetry (LSV) curves of all obtained electrocatalysts with iR compensation. The designed Fe-Ni-P shows remarkable OER performance with 188 and 237 mV to reach 10 and 50 mA·cm^{-2}, superior to NiFe (348 and 408 mV), NiFe LDH (280 and 313 mV), and RuO_2 (288 and 323 mV), confirming that its excellent OER performance. The Fe-Ni-P shows a Tafel slope of 23 mV·dec^{-1}, smaller than NiFe LDH (40 mV·dec^{-1}), NiFe (64 mV·dec^{-1}), and RuO_2 (42 mV·dec^{-1}), verifying its favorable kinetics (Figs. 5(b) and 5(c)). Remarkably, the catalytic activity of Fe-Ni-P is comparable or even superior to some recently reported OER electrocatalysts (Fig. 5(d)). It can be seen in Fig. 5(e) that the current densities maintained well during the measurement, proving its excellent durability and mass transfer properties. Meanwhile, the chronopotentiometry measurement also verifies its excellent durability (Fig. 5(f)). In addition, the phosphorization temperature and the content of phosphorous resource were explored for optimizing performance (Fig. S7 in the ESM).

3.4 Measurement for overall water-splitting

In consideration of the bifunctional electrocatalytic activities toward HER and OER, the overall water splitting system is assembled with the self-supporting Fe-Ni-P as anodic and Ru-Fe-Ni-P as cathodic electrodes simultaneously (inset in Fig. 6(a)). The LSV curves in Fig. 6(a) show that the electrolyzer needs a potential of 1.51 V to achieve 10 mA·cm^{-2}, which is superior to Pt-C/NiFe||RuO_2/NiFe (1.6 V). Evidently, sumless O_2 and H_2 bubbles

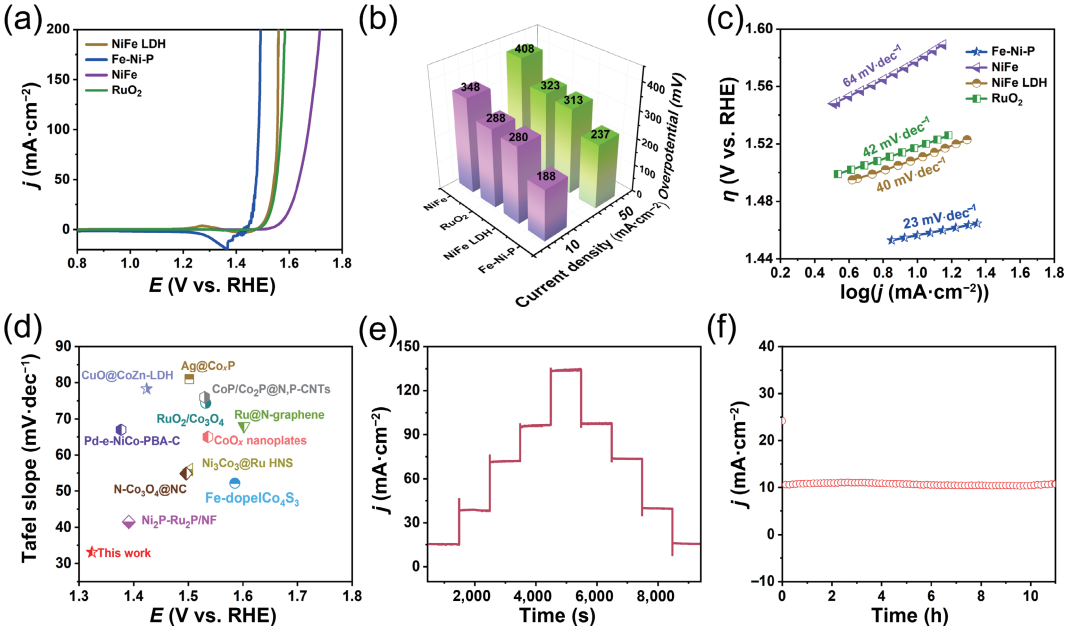

Figure 5 Electrochemical activities toward OER in 1 M KOH. (a) LSV curves of NiFe, NiFe LDH, Fe-Ni-P, and RuO_2. (b) Comparison of corresponding overpotentials at 10 and 50 mA·cm^{-2}. (c) Tafel plots of NiFe, NiFe LDH, Fe-Ni-P, and RuO_2 for OER. (d) Comparison of overpotentials at 10 mA·cm^{-2} with reported catalysts. (e) The durability test of the Fe-Ni-P with different potentials. (f) Long-term stability test of Fe-Ni-P at the current density of 10 mA·cm^{-2}.

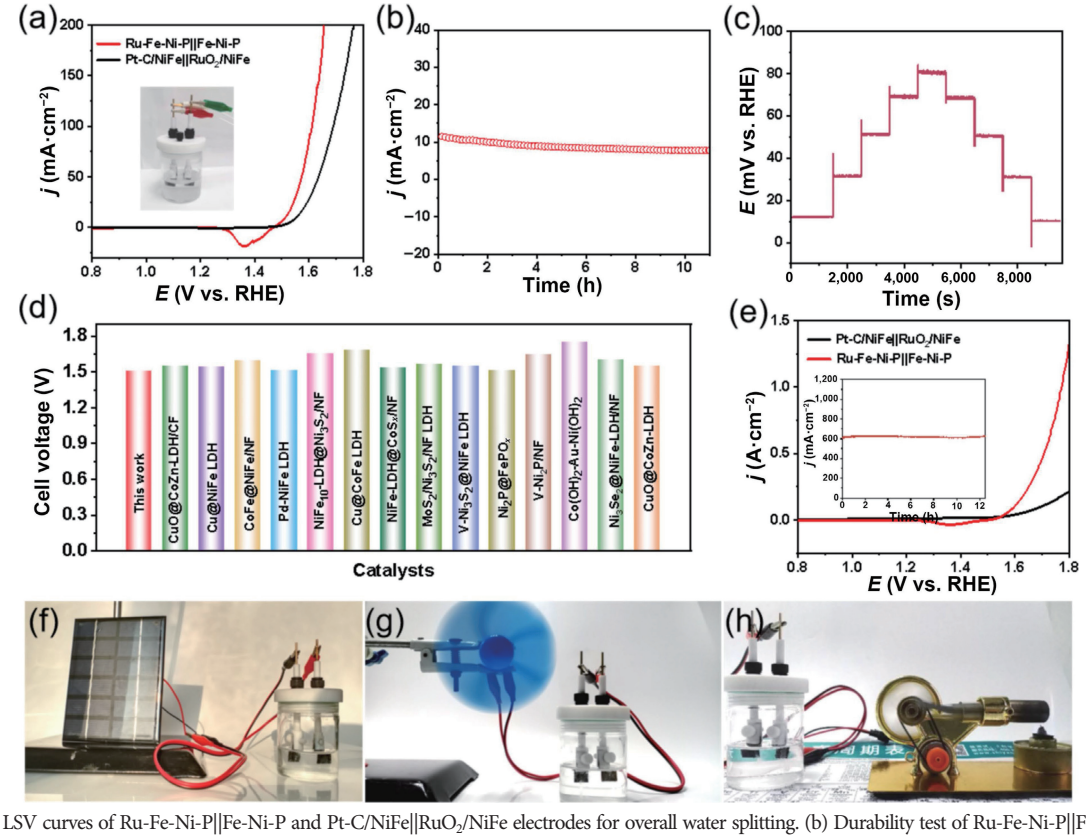

Figure 6 (a) LSV curves of Ru-Fe-Ni-P||Fe-Ni-P and Pt-C/NiFe||RuO_2/NiFe electrodes for overall water splitting. (b) Durability test of Ru-Fe-Ni-P||Fe-Ni-P under a constant overpotential of 10 mA·cm^{-2}. (c) Chronoamperometry curve of the Ru-Fe-Ni-P||Fe-Ni-P in 1 M KOH. (d) Comparison of the electrochemical overall water splitting activities between the prepared Ru-Fe-Ni-P||Fe-Ni-P with recently reported catalysts in 1 M KOH. (e) LSV curves of Ru-Fe-Ni-P||Fe-Ni-P and Pt-C/NiFe||RuO_2/NiFe electrodes. Photograph of the Ru-Fe-Ni-P||Fe-Ni-P electrolyzer driven by the (f) solar energy, (g) Stirling engine, and (h) wind.

were generated from the two electrodes (Movie ESM2). Moreover, the chronoamperometric and multi-step chronopotentiometry measurements demonstrate the Ru-Fe-Ni-P||Fe-Ni-P electrolyzer exhibits excellent stability (Figs. 6(b) and 6(c)). Remarkably, the electrolyzer consisting of Ru-Fe-Ni-P and Fe-Ni-P presents a remarkable electrocatalytic activity toward water-splitting, superior to many reported available catalysts (Fig. 6(d) and Table S4 in the ESM). As illustrated in Fig. 6(e), only a small voltage of 1.65 V is required to achieve 600 mA·cm^{-2} of the electrolyzer composed of Ru-Fe-Ni-P||Fe-Ni-P with excellent stability. Then, due to its excellent catalytic properties, the electrolyzer can be powered by solar energy, wind energy, Stirling engine, and battery-driven successfully (Figs. 6(f)–6(h), Fig. S8 in the ESM, and Movies ESM3–6), proving that the designed catalysts have widely industrial application prospect in large scale hydrogen production.

4 Conclusions

In summary, a self-supported porous Fe-Ni-P and Ru-Fe-Ni-P electrocatalyst are developed via a facile strategy for highly efficient water splitting. Owing to the successful synthesis of phosphides and the incorporation of a few Ru, the prepared composite material act as an outstanding catalyst for improving the HER and OER performances in alkaline and neutral media. Remarkably, the designed nanomaterial owns excellent catalytic activity for water-splitting with splendid stability, which can be driven by thermal, solar, and wind energies. Additionally, a porous structure can expose more of the active site and good hydrophilia is favorable to improve catalytic performance. Consequently, the developed catalysts achieved an excellent performance toward HER, OER, and water splitting, and then accelerated the development on large-scale water splitting by electrolysis.

Acknowledgements

The authors acknowledge funding support from the National Natural Science Foundation of China (Nos. 22002068, 21971132, 51772162, and 52072197), a project funded by China Postdoctoral Science Foundation (No. 2021M691700), Youth Innovation and Technology Foundation of Shandong Higher Education Institutions, China (No. 2019KJC004), Outstanding Youth Foundation of Shandong Province, China (No. ZR2019JQ14), Taishan Scholar Young Talent Program (No. tsqn201909114), Major Scientific and Technological Innovation Project (No. 2019JZZY020405), Major Basic Research Program of Natural Science Foundation of Shandong Province (No. ZR2020ZD09), the Natural Science Foundation of Shandong Province of China (Nos. ZR2019BB002 and ZR2018BB031), and Talent Foundation funded by Province and Ministry Co-construction Collaborative Innovation Center of Eco-chemical Engineering (No. STHGYX2202).

Electronic Supplementary Material: Supplementary material (further details of XRD, XPS spectrograms of Ru-Fe-Ni-P and Fe-Ni-P, as well as LSV plots of the property probes are presented) is available in the online version of this article at https://doi.org/10.1007/s12274-022-4980-4.

References

[1] Gong, L. Q.; Yang, H.; Wang, H. M.; Qi, R. J.; Wang, J. L.; Chen, S. H.; You, B.; Dong, Z. H.; Liu, H. F.; Xia, B. Y. Corrosion formation and phase transformation of nickel-iron hydroxide nanosheets array for efficient water oxidation. *Nano Res.* **2021**, *14*, 4528–4533.

[2] Yu, W. L.; Gao, Y. X.; Chen, Z.; Zhao, Y.; Wu, Z. X.; Wang, L. Strategies on improving the electrocatalytic hydrogen evolution performances of metal phosphides. *Chin. J. Catal.* **2021**, *42*, 1876–1902.

[3] Wang, X.; Zhang, X. Y.; Fu, G. T.; Tang, Y. W. Recent progress of electrospun porous carbon-based nanofibers for oxygen electrocatalysis. *Mater. Today Energy* **2021**, *22*, 100850.

[4] Niu, S. W.; Cai, J. Y.; Wan, G. M. Two-dimensional MoS_2 for hydrogen evolution reaction catalysis: The electronic structure regulation. *Nano Res.* **2021**, *14*, 1985–2002.

[5] Wang, H. Q. Nanostructure@metal–organic frameworks (MOFs) for catalytic carbon dioxide (CO_2) conversion in photocatalysis, electrocatalysis, and thermal catalysis. *Nano Res.* **2022**, *15*, 2834–2854.

[6] Wang, H. Q.; Xu, J. H.; Zhang, Q. H.; Hu, S. X.; Zhou, W. J.; Liu, H.; Wang, X. Super-hybrid transition metal sulfide nanoarrays of Co_3S_4 nanosheet/P-doped WS_2 nanosheet/Co_9S_8 nanoparticle with Pt-like activities for robust all-pH hydrogen evolution. *Adv. Funct. Mater.* **2022**, *32*, 2112362.

[7] Xiong, Y.; Sun, W. M.; Han, Y. H.; Xin, P. Y.; Zheng, X. S.; Yan, W. S.; Dong, J. C.; Zhang, J.; Wang, D. S.; Li, Y. D. Cobalt single atom site catalysts with ultrahigh metal loading for enhanced aerobic oxidation of ethylbenzene. *Nano Res.* **2021**, *24*, 2418–2423.

[8] Song, H. R.; Wang, J. S.; Zhang, Z. F.; Shai, X. X.; Guo, Y. Z. Synergistic balancing hydrogen and hydroxyl adsorption/desorption of nickel sulfide via cation and anion dual-doping for boosting alkaline hydrogen evolution. *Chem. Eng. J.* **2021**, *420*, 129842.

[9] Guo, X.; Wan, X.; Liu, Q. T.; Li, Y. C.; Li, W. W.; Shui, J. L. Phosphated IrMo bimetallic cluster for efficient hydrogen evolution reaction. *eScience* **2022**, *2*, 304–310.

[10] Hu, B. T.; Huang, A. J.; Zhang, X. J.; Chen, Z.; Tu, R. Y.; Zhu, W.; Zhuang, Z. B.; Chen, C.; Peng, Q.; Li, Y. D. Atomic Co/Ni dual sites with N/P-coordination as bifunctional oxygen electrocatalyst for rechargeable zinc–air batteries. *Nano Res.* **2021**, *14*, 3482–3488.

[11] Wu, W. J.; Liu, Y.; Liu, D.; Chen, W. X.; Song, Z. Y.; Wang, X. M.; Zheng, Y. M.; Lu, N.; Wang, C. X.; Mao, J. J. et al. Single copper sites dispersed on hierarchically porous carbon for improving oxygen reduction reaction towards zinc–air battery. *Nano Res.* **2021**, *14*, 998–1003.

[12] Chen, L.; Chen, Z.; Liu, X. D.; Wang, X. L. Bimetallic metal–organic framework derived doped carbon nanostructures as high-performance electrocatalyst towards oxygen reactions. *Nano Res.* **2021**, *14*, 1533–1540.

[13] Wang, J. S.; Zhang, Z. F.; Song, H. R.; Zhang, B.; Liu, J.; Shai, X. X.; Miao, L. Water dissociation kinetic-oriented design of nickel sulfides via tailored dual sites for efficient alkaline hydrogen evolution. *Adv. Funct. Mater.* **2021**, *31*, 2008578.

[14] Zhang, X. Y.; Liu, T. Y.; Guo, T.; Han, X. Y.; Mu, Z. Y.; Chen, Q.; Jiang, J. M.; Yan, J.; Yuan, J. R.; Wang, D. Z. et al. Controlling atomic phosphorous-mounting surfaces of ultrafine W_2C nanoislands monodispersed on the carbon frameworks for enhanced hydrogen evolution. *Chin. J. Catal.* **2021**, *42*, 1798–1807.

[15] Wu, Y. T.; Wang, H.; Ji, S.; Pollet, B. G.; Wang, X. Y.; Wang, R. F. Engineered porous Ni_2P-nanoparticle/Ni_2P-nanosheet arrays via the Kirkendall effect and Ostwald ripening towards efficient overall water splitting. *Nano Res.* **2020**, *13*, 2098–2105.

[16] Li, M.; Li, H.; Jiang, X. C.; Jiang, M. Q.; Zhan, X.; Fu, G. T.; Lee, J. M.; Tang, Y. W. Gd-induced electronic structure engineering of a NiFe-layered double hydroxide for efficient oxygen evolution. *J. Mater. Chem. A* **2021**, *9*, 2999–3006.

[17] Deng, L. M.; Hu, F.; Ma, M. Y.; Huang, S. C.; Xiong, Y. X.; Chen, H. Y.; Li, L. L.; Peng, S. J. Electronic modulation caused by interfacial Ni–O–M (M = Ru, Ir, and Pd) bonding for accelerating hydrogen evolution kinetics. *Angew. Chem.* **2021**, *133*, 22450–22456.

[18] Yu, Z. Y.; Duan, Y.; Feng, X. Y.; Yu, X. X.; Gao, M. R.; Yu, S. H. Clean and affordable hydrogen fuel from alkaline water splitting: Past, recent progress, and future prospects. *Adv. Mater.* **2021**, *33*, 2007100.

[19] Wang, C.; Li, W.; Wang, X. D.; Yu, N.; Sun, H. X.; Geng, B. Y. Open N-doped carbon coated porous molybdenum phosphide nanorods for synergistic catalytic hydrogen evolution reaction. *Nano Res.* **2022**, *15*, 1824–1830.

[20] Zhao, G.; Ma, W. X.; Wang, X. K.; Xing, Y. P.; Hao, S. H.; Xu, X. J. Self-water-absorption-type two-dimensional composite photocatalyst with high-efficiency water absorption and overall water-splitting performance. *Adv. Powder Mater.* **2022**, *1*, 100008.

[21] Chen, Z.; Liu, D. Z.; Gao, Y. X.; Zhao, Y.; Xiao, W. P.; Xu, G. R.; Ma, T. Y.; Wu, Z. X.; Wang, L. Corrosive-coordinate engineering to construct 2D–3D nanostructure with trace Pt as efficient bifunctional electrocatalyst for overall water splitting. *Sci. China Mater.* **2022**, *65*, 1217–1224.

[22] Du, J. L.; Yu, H. H.; Liu, B. S.; Hong, M. Y.; Liao, Q. L.; Zhang, Z.; Zhang, Y. Strain engineering in 2D material-based flexible optoelectronics. *Small Methods* **2021**, *5*, 2000919.

[23] Li, S. H.; Qi, M. Y.; Tang, Z. R.; Xu, Y. J. Nanostructured metal phosphides: From controllable synthesis to sustainable catalysis. *Chem. Soc. Rev.* **2021**, *50*, 7539–7586.

[24] Li, Z. J.; Wu, X. D.; Jiang, X.; Shen, B. B.; Teng, Z. S.; Sun, D. M.; Fu, G. T.; Tang, Y. W. Surface carbon layer controllable Ni_3Fe particles confined in hierarchical N-doped carbon framework

boosting oxygen evolution reaction. *Adv. Powder Mater.* **2022**, *1*, 100020.
[25] Zhang, A.; Liang, Y. X.; Zhang, H.; Geng, Z. G.; Zeng, J. Doping regulation in transition metal compounds for electrocatalysis. *Chem. Soc. Rev.* **2021**, *50*, 9817–9844.
[26] Hu, F.; Yu, D. S.; Ye, M.; Wang, H.; Hao, Y. N.; Wang, L. Q.; Li, L. L.; Han, X. P.; Peng, S. J. Lattice-matching formed mesoporous transition metal oxide heterostructures advance water splitting by active Fe-O-Cu bridges. *Adv. Energy Mater.* **2022**, *12*, 2200067.
[27] Kang, T.; Kim, K.; Kim, M.; Kim, J. Synergistic metal–oxide interaction for efficient self-reconstruction of cobalt oxide as highly active water oxidation electrocatalyst. *J. Catal.* **2021**, *404*, 80–88.
[28] Lai, Y. Q.; Zhang, Z. T.; Zhang, Z. Y.; Tan, Y. Y.; Yu, L. Y.; Wu, W.; Wang, Z. C.; Jiang, T.; Gao, S. H.; Cheng, N. C. Electronic modulation of Pt nanoclusters through tuning the interface of Pt-SnO_2 clusters for enhanced hydrogen evolution catalysis. *Chem. Eng. J.* **2022**, *435*, 135102.
[29] Wang, W.; Wang, Z. X.; Hu, Y. C.; Liu, Y. C.; Chen, S. L. A potential-driven switch of activity promotion mode for the oxygen evolution reaction at Co_3O_4/NiO_xH_y interface. *eScience* **2022**, *2*, 438–444.
[30] Li, S. X.; Liang, J.; Wei, P. P.; Liu, Q.; Xie, L. S.; Luo, Y. L.; Sun, X. P. ITO@TiO_2 nanoarray: An efficient and robust nitrite reduction reaction electrocatalyst toward NH_3 production under ambient conditions. *eScience* **2022**, *2*, 382–388.
[31] Zhang, H. J.; Maijenburg, A. W.; Li, X. P.; Schweizer, S. L.; Wehrspohn, R. B. Bifunctional heterostructured transition metal phosphides for efficient electrochemical water splitting. *Adv. Funct. Mater.* **2020**, *30*, 2003261.
[32] Xu, Y. Y.; Duan, S. B.; Li, H. Y.; Yang, M.; Wang, S. J.; Wang, X.; Wang, R. M. Au/$Ni_{12}P_5$ core/shell single-crystal nanoparticles as oxygen evolution reaction catalyst. *Nano Res.* **2017**, *10*, 3103–3112.
[33] Men, Y. N.; Tan, Y.; Li, P.; Cao, X. M.; Jia, S. F.; Wang, J. B.; Chen, S. L.; Luo, W. Tailoring the 3d-orbital electron filling degree of metal center to boost alkaline hydrogen evolution electrocatalysis. *Appl. Catal. B: Environ.* **2021**, *284*, 119718.
[34] Yang, C. F.; Zhao, R.; Xiang, H.; Wu, J.; Zhong, W. D.; Li, W. L.; Zhang, Q.; Yang, N. J.; Li, X. K. Ni-activated transition metal carbides for efficient hydrogen evolution in acidic and alkaline solutions. *Adv. Energy Mater.* **2020**, *10*, 2002260.
[35] Chen, P. R.; Ye, J. S.; Wang, H.; Ouyang, L. Z.; Zhu, M. Recent progress of transition metal carbides/nitrides for electrocatalytic water splitting. *J. Alloys Compd.* **2021**, *883*, 160833.
[36] Li, M. R.; Zheng, K. T.; Zhang, J. J.; Li, X. M.; Xu, C. J. Design and construction of 2D/2D sheet-on-sheet transition metal sulfide/phosphide heterostructure for efficient oxygen evolution reaction. *Appl. Surf. Sci.* **2021**, *565*, 150510.
[37] Han, H. C.; Yang, J. J.; Li, X. Y.; Qi, Y.; Yang, Z. Y.; Han, Z. J.; Jiang, Y. Y.; Stenzel, M.; Li, H.; Yin, Y. X. et al. Shining light on transition metal sulfides: New choices as highly efficient antibacterial agents. *Nano Res.* **2021**, *14*, 2512–2534.
[38] Sun, Y. K.; Liu, T.; Li, Z. J.; Meng, A. L.; Li, G. C.; Wang, L.; Li, S. X. Morphology and interfacial charge regulation strategies constructing 3D flower-like Co@CoP_2 heterostructure electrocatalyst for efficient overall water splitting. *Chem. Eng. J.* **2022**, *433*, 133684.
[39] Chinnadurai, D.; Rajendiran, R.; Li, O. L.; Prabakar, K. Mn-Co bimetallic phosphate on electrodeposited PANI nanowires with composition modulated structural morphology for efficient electrocatalytic water splitting. *Appl. Catal. B: Environ.* **2021**, *292*, 120202.
[40] Yang, Q. F.; Jin, P.; Liu, B.; Zhao, L.; Cai, J. H.; Wei, Z.; Zuo, S. W.; Zhang, J.; Feng, L. Ultrafine carbon encapsulated NiRu alloys as bifunctional electrocatalysts for boosting overall water splitting: Morphological and electronic modulation through minor Ru alloying. *J. Mater. Chem. A* **2020**, *8*, 9049–9057.
[41] Hao, S. Y.; Chen, L. C.; Yu, C. L.; Yang, B.; Li, Z. J.; Hou, Y.; Lei, L. C.; Zhang, X. W. NiCoMo hydroxide nanosheet arrays synthesized via chloride corrosion for overall water splitting. *ACS Energy Lett.* **2019**, *4*, 952–959.
[42] Yu, X. W.; Zhao, J.; Johnsson, M. Interfacial engineering of nickel hydroxide on cobalt phosphide for alkaline water electrocatalysis. *Adv. Funct. Mater.* **2021**, *31*, 2101578.
[43] Bian, X. J.; Zhu, J.; Liao, L.; Scanlon, M. D.; Ge, P. Y.; Ji, C.; Girault, H. H.; Liu, B. H. Nanocomposite of MoS_2 on ordered mesoporous carbon nanospheres: A highly active catalyst for electrochemical hydrogen evolution. *Electrochem. Commun.* **2012**, *22*, 128–132.
[44] Pei, H. J.; Zhang, L. M.; Zhi, G.; Kong, D. Z.; Wang, Y.; Huang, S. Z.; Zang, J. H.; Xu, T. T.; Wang, H.; Li, X. J. Rational construction of hierarchical porous FeP nanorod arrays encapsulated in polypyrrole for efficient and durable hydrogen evolution reaction. *Chem. Eng. J.* **2022**, *433*, 133643.
[45] Liu, C. C.; Han, Y.; Yao, L. B.; Liang, L. M.; He, J. Y.; Hao, Q. Y.; Zhang, J.; Li, Y.; Liu, H. Engineering bimetallic NiFe-based hydroxides/selenides heterostructure nanosheet arrays for highly-efficient oxygen evolution reaction. *Small* **2021**, *17*, 2007334.
[46] Wang, F.; Niu, S. W.; Liang, X. Q.; Wang, G. M.; Chen, M. H. Phosphorus incorporation activates the basal plane of tungsten disulfide for efficient hydrogen evolution catalysis. *Nano Res.* **2022**, *15*, 2855–2861.
[47] Xue, H. Y.; Meng, A. L.; Zhang, H. Q.; Lin, Y. S.; Li, Z. J.; Wang, C. S. 3D urchin like V-doped CoP *in-situ* grown on nickel foam as bifunctional electrocatalyst for efficient overall water-splitting. *Nano Res.* **2021**, *14*, 4173–4181.
[48] Zhou, S. Q.; Yang, Y. T.; Zhang, W. Y.; Rao, X. F.; Yan, P. X.; Isimjan, T. T.; Yang, X. L. Structure-regulated Ru particles decorated P-vacancy-rich CoP as a highly active and durable catalyst for $NaBH_4$ hydrolysis. *J. Colloid Interface Sci.* **2021**, *591*, 221–228.
[49] Li, J. C.; Zhang, C.; Zhang, C.; Ma, H. J.; Guo, Z. Q.; Zhong, C. L.; Xu, M.; Wang, X. J.; Wang, Y. Y.; Ma, H. X. et al. Green electrosynthesis of 5, 5′-azotetrazolate energetic materials plus energy-efficient hydrogen production using ruthenium single-atom catalysts. *Adv. Mater.* **2022**, *34*, 2203900.
[50] Kim, D.; Qin, X. Y.; Yan, B. Y.; Piao, Y. Z. Sprout-shaped Mo-doped CoP with maximized hydrophilicity and gas bubble release for high-performance water splitting catalyst. *Chem. Eng. J.* **2021**, *408*, 127331.
[51] Fereja, S. L.; Li, P.; Zhang, Z. W.; Guo, J. H.; Fang, Z. Y.; Li, Z. J.; He, S. J.; Chen, W. W-doping induced abundant active sites in a 3D NiS_2/MoO_2 heterostructure as an efficient electrocatalyst for urea oxidation and hydrogen evolution reaction. *Chem. Eng. J.* **2022**, *432*, 134274.
[52] Wei, C. B.; Fan, X. M.; Deng, X.; Ma, L. Z.; Zhang, X.; Liu, Q. Y.; Guo, J. X. Ruthenium doped Ni_2P nanosheet arrays for active hydrogen evolution in neutral and alkaline water. *Sustainable Energy Fuels* **2020**, *4*, 1883–1890.
[53] You, B.; Zhang, Y. D.; Jiao, Y.; Davey, K.; Qiao, S. Z. Negative charging of transition-metal phosphides via strong electronic coupling for destabilization of alkaline water. *Angew. Chem.* **2019**, *131*, 11922–11926.
[54] Wang, K. W.; She, X. L.; Chen, S.; Liu, H. L.; Li, D. H.; Wang, Y.; Zhang, H. W.; Yang, D. J.; Yao, X. D. Boosting hydrogen evolution via optimized hydrogen adsorption at the interface of CoP_3 and Ni_2P. *J. Mater. Chem. A* **2018**, *6*, 5560–5565.
[55] Han, W. F.; Li, X. L.; Liu, B.; Li, L. C.; Tang, H. D.; Li, Y.; Lu, C. S.; Li, X. N. Microwave assisted combustion of phytic acid for the preparation of Ni_2P@C as a robust catalyst for hydrodechlorination. *Chem. Commun.* **2019**, *55*, 9279–9282.
[56] Li, D.; Li, Z. Y.; Zou, R.; Shi, G.; Huang, Y. M.; Yang, W.; Yang, W.; Liu, C. F.; Peng, X. W. Coupling overall water splitting and biomass oxidation via Fe-doped Ni_2P@C nanosheets at large current density. *Appl. Catal. B: Environ.* **2022**, *307*, 121170.
[57] Li, Y.; Pan, Y.; Zhang, J. *In-situ* grown of Ni_2P nanoparticles on 2D black phosphorus as a novel hybrid catalyst for hydrogen evolution. *Int. J. Hydrog. Energy* **2017**, *42*, 7951–7956.
[58] Zhang, R.; Wang, G. D.; Wei, Z. H.; Teng, X.; Wang, J. J.; Miao, J. J.; Wang, Y. H.; Yang, F. X.; Zhu, X. W.; Chen, C. F. et al. A Fe–Ni_5P_4/Fe–Ni_2P heterojunction electrocatalyst for highly efficient solar-to-hydrogen generation. *J. Mater. Chem. A* **2021**, *9*,

1221–1229.

[59] Liang, Y. H.; Liu, Q.; Asiri, A. M.; Sun, X. P.; Luo, Y. L. Self-supported FeP nanorod arrays: A cost–effective 3D hydrogen evolution cathode with high catalytic activity. *ACS Catal.* **2014**, *4*, 4065–4069.

[60] Liu, Y.; Zhen, W. Y.; Wang, Y. H.; Liu, J. H.; Jin, L. H.; Zhang, T. Q.; Zhang, S. T.; Zhao, Y.; Song, S. Y.; Li, C. Y. et al. One-dimensional Fe_2P acts as a Fenton agent in response to NIR II light and ultrasound for deep tumor synergetic theranostics. *Angew. Chem.* **2019**, *131*, 2429–2434.

[61] Lyu, M.; Zhu, D. M.; Kong, X. Y.; Yang, Y.; Ding, S. J.; Zhou, Y. F.; Quan, H.; Duo, Y. H.; Bao, Z. R. Glutathione-depleting nanoenzyme and glucose oxidase combination for hypoxia modulation and radiotherapy enhancement. *Adv. Healthc. Mater.* **2020**, *9*, 1901819.

[62] Shi, X. L.; An, P. F.; Zhang, Q.; Song, Q.; Jiang, D. L.; Tian, D.; Li, D. Synergy of nitrogen vacancies and Fe_2P cocatalyst on graphitic carbon nitride for boosting photocatalytic CO_2 conversion. *Chem. Eng. J.* **2022**, *446*, 137096.

[63] Drouet, S.; Creus, J.; Collière, V.; Amiens, C.; García-Antón, J.; Sala, X.; Philippot, K. A porous Ru nanomaterial as an efficient electrocatalyst for the hydrogen evolution reaction under acidic and neutral conditions. *Chem. Commun.* **2017**, *53*, 11713–11716.

[64] Zhao, Z. F.; Wu, Z. J.; Zhou, L. X.; Zhang, M. H.; Li, W.; Tao, K. Y. Synthesis of a nano-nickel catalyst modified by ruthenium for hydrogenation and hydrodechlorination. *Catal. Commun.* **2008**, *9*, 2191–2194.

[65] Su, L.; Cui, X. Z.; He, T.; Zeng, L. M.; Tian, H.; Song, Y. L.; Qi, K.; Xia, B. Y. Surface reconstruction of cobalt phosphide nanosheets by electrochemical activation for enhanced hydrogen evolution in alkaline solution. *Chem. Sci.* **2019**, *10*, 2019–2024.